Hard antiphase domain boundaries in strontium titanate unravelled using machine-learned force fields

A. Tröster [1,*] C. Verdi [1] C. Dellago [1] I. Rychetsky [2] G. Kresse [1] and W. Schranz [1]

[1] *University of Vienna, Faculty of Physics, Boltzmanngasse 5, A-1090 Vienna, Austria*

[2] *Institute of Physics, Academy of Sciences of the Czech Republic, Na Slovance 2, 18221 Prague 8, Czech Republic*

(Received 10 December 2021; revised 16 August 2022; accepted 6 September 2022; published 16 September 2022)

We investigate the properties of hard antiphase boundaries in $SrTiO_3$ using machine-learned force fields. In contrast to earlier findings based on standard *ab initio* methods, for all pressures up to 120 kbar the observed domain wall pattern maintains an almost perfect Néel character in quantitative agreement with Landau-Ginzburg-Devonshire theory, and the in-plane polarization P_3 shows no tendency to decay to zero. Together with the switching properties of P_3 under reversal of the Néel order parameter component, this provides hard evidence for the presence of rotopolar couplings. The present approach overcomes the severe limitations of *ab initio* simulations of wide domain walls and opens avenues toward concise atomistic predictions of domain-wall properties even at finite temperatures.

DOI: 10.1103/PhysRevMaterials.6.094408

I. INTRODUCTION

Recently, the focus of research on ferroic materials has shifted from bulk [1,2] to domains [3] and finally to domain walls (DWs) [4–8]. The discovery of domain wall properties like vastly increased conductivity [9], superconductivity [10], ferrielectricity, and ferroelectricity [11–15] has stirred up much attention [16] for their potential use in nanoelectronics [17,18]. The fact that DWs in ferroics may be created, moved around, annihilated, and recreated nourishes hopes for greatly enhanced flexibility of future electronic devices created by what is nowadays called domain wall engineering as compared to the functionality offered by conventional static heterointerfaces between metal oxides. In all this research, however, theoretically predicting the atomistic structure of a DW and its stability range with respect to pressure and temperature is a key aspect that is often very difficult to address.

Antiphase boundaries (APBs) between nonpolar bulk phases (see below for an explanation of this terminology) are regarded as especially interesting due to their ability to carry a nonzero polarization [19] that can be switched upon reversal of an external electric field, a key property for possible use in ferroelectric (FE) devices. A prime example is the archetypal perovskite $SrTiO_3$ (STO), for which the existence of a switchable polarization in APBs was predicted based on a phenomenological Landau-Ginzburg-Devonshire (LGD) approach [20]. Recall that at $T_s = 105$ K, STO undergoes a well-studied antiferrodistortive (AFD) phase transition $Pm\bar{3}m \rightarrow I4/mcm$. Its three-dimensional order parameter (OP) components ϕ_i, $i = 1, 2, 3$ resemble the amplitudes of three AFD soft modes of R_{25} symmetry [21] corresponding to alternating rotation angles of the TiO_6 octahedra around the three cubic unit cell axes. Besides this R_{25} instability, however, *ab initio* calculations [22] also exhibit a polar FE soft mode of Γ_{15} symmetry. Indeed, STO would undergo a further low-temperature transition to a FE state around $T_f \sim 30$ K, which is only suppressed by a combination of quantum fluctuations [23] and a competition between the AFD and FE modes [24]. In LGD theory, the latter is encoded by a repulsive biquadratic coupling $\sim\phi_3^2 P_3^2$ [20,25]. Due to the symmetry reduction at the phase transition, the tetragonal phase can appear in 6 domain states labeled S_i. In this short-hand notation [26,27], S distinguishes three different orientational states $1 = (\bar{\phi}, 0, 0)$, $2 = (0, \bar{\phi}, 0)$, $3 = (0, 0, \bar{\phi})$ and the subscript i specifies the translational state within each orientational state, e.g., $1_1 = (\bar{\phi}, 0, 0)$, $1_2 = (-\bar{\phi}, 0, 0)$, etc., where $\bar{\phi}$ denotes the modulus of the spontaneous bulk OP. A "hard" APB results from gluing together, e.g., 3_1 and 3_2 with the DW plane normal to (1,0,0). In OP space, any continuous local OP profile $(0, 0, \phi_3(x_1))$ across such a hard APB must vanish at its center for symmetry reasons. Thus, the effectiveness of the $\phi_3^2 P_3^2$ coupling suppressing the FE mode will break down inside the APB, and a FE phase transition at T_f may occur in the vicinity of its center. Moreover, LGD calculations by Tagantsev *et al.* [20] predicted that hard APBs in STO develop an additional (Néel) component $\phi_1(x)$ with an amplitude that peaks at almost $\bar{\phi}$ in the DW center. Interestingly, however, subsequent density functional theory (DFT)-based calculations of APBs [28] exhibit several discrepancies with these LGD results. In particular, although the prediction of an emergent nonzero Néel-type component $\phi_1(x)$ was verified, its amplitude was only a small fraction of that obtained from LGD theory [20] and the observed width of the hard APB was much smaller. Conventional DFT approaches are, however, seriously limited by the accessible system size. This is especially critical in the present case of a hard APB, where geometrical frustration between the octahedra on both sides of the wall causes such walls to spread out over many pseudocubic lattice constants. Hence, it seems crucial to devise a more efficient general

*andreas.troester@univie.ac.at

framework for predictive atomistic calculations of DW properties.

In recent years, machine-learned force fields (MLFFs) [29,30] have emerged as a powerful tool to explore the potential energy landscape of materials at a small fraction of the cost of first-principles calculations, but retaining almost the same accuracy. In the present paper, we calculate the structure and properties of hard APBs in STO using an on-the-fly kernel-based MLFF [31–33]. This allows us to perform careful and accurate relaxations in supercells of sizes that were previously far beyond the reach of direct first-principles calculations. The resulting DW profiles are analyzed in terms of local phonon and polarization amplitudes at different pressures and are put into perspective with corresponding results obtained numerically from LGD theory.

The outline of the remaining part of the paper is as follows. We start with a brief discussion of the DFT and ML approaches used. This is followed by a review of our supercell setup and the structural relaxation of DW profiles. The structural OP and polarization amplitudes carried by the resulting DW profiles are discussed. Finally, we present evidence for the presence of so-called rotopolar coupling terms beyond the biquadratic ones in LGD phenomenology of hard APBs.

II. FIRST-PRINCIPLES CALCULATIONS AND MLFF TRAINING

Let us start with a brief account of the MLFF method used throughout the paper.

By mapping structural features onto a set of descriptors, MLFF models can simultaneously predict the energy, atomic forces, and stress tensor components of a given system. In this paper, we adopt the Gaussian approximation potential [34] approach, where each local atomic energy is expressed as a linear combination of kernel functions, and we use Bayesian linear regression to determine the weighting coefficients. We employ an efficient on-the-fly training method [35], where the first-principles training data are collected during molecular dynamics (MD) simulations. In practice, only when the estimated Bayesian error of the MLFF is larger than a specified threshold, a first-principles calculation is performed and the corresponding data are added to the training set, allowing to refine the MLFF. A detailed description of the MLFF model, the descriptors, and the on-the-fly training procedure can be found in Refs. [32,33].

All DFT and MLFF calculations, including the MLFF training, are performed using VASP [36,37], while for phonon calculations we use the PHONOPY package [38]. The MLFF is trained on the fly during MD simulations in the NpT ensemble with a time step of 2 fs. A supercell containing 320 atoms is first heated from 150 K to 350 K at ambient pressure in 150 ps, then starting from 10 K to 150 K in another 150 ps. Additional data are gathered at $p = 40$ kbar and $p = 100$ kbar for 100 ps. The training data set thus generated consists of 831 structures and their relative first-principles energies, forces, and stress tensors. The first-principles calculations are performed using the PBEsol exchange-correlation functional, a plane-wave cutoff of 700 eV, and a $2 \times 2 \times 2$ Monkhorst-Pack k-mesh for the 320-atom supercell.

TABLE I. Lattice constants and energy differences (per formula unit) of the ideal cubic and tetragonal phases at $P = 0$ and 40 kbar, calculated from DFT (PBEsol) and MLFF.

	$P = 0$ kbar		$P = 40$ kbar	
	PBEsol	MLFF	PBEsol	MLFF
Cubic				
a (Å)	3.8934	3.8924	3.8645	3.8649
$\Delta E_{\text{c-t}}$ (meV)	4.5	4.5	4.1	3.8
Tetragonal				
a (Å)	3.8848	3.8842	3.8531	3.8533
c (Å)	3.9040	3.9040	3.8791	3.8796
c/a	1.005	1.005	1.007	1.007

To calculate the descriptors, we set the cutoff radius used to represent the local environment of each atom to 6 Å, while the Gaussian broadening for the atomic distribution functions is 0.2 Å. As radial and angular basis functions, we use up to 22 spherical Bessel functions and Legendre polynomials up to order $l = 4$, respectively. The same parameters are used for the two- and three-body descriptors. We use a polynomial kernel with hyperparameter $\zeta = 4$ (Ref. [39]), and we train the MLFF by weighing energy, force, and stress data equally when solving the Bayesian regression problem. The resulting MLFF yields root-mean-square errors in the energies, forces, and stress tensors for the training data set of 0.53 meV/atom, 0.03 eV/Å, and 0.50 kbar, respectively. The calculated zero-temperature lattice parameters of the ideal cubic and tetragonal phase are reported in Table I, both from DFT and the MLFF, which are in almost perfect agreement. As a further test of the quality of the MLFF predictions, we show the phonon dispersions and the double-well potential from the FE instability in the tetragonal phase, calculated from first-principles and from the MLFF (Figs. 1 and 2).

III. DOMAIN-WALL SUPERCELL SETUP AND STRUCTURAL RELAXATION

In setting up the supercells needed to perform our DW simulations, care is needed to establish compatibility of the DW structure with the periodic boundary conditions that are mandatory for DFT calculations. Taking the DW normal pointing along x_1 and the primary OP pointing along x_3, it obviously suffices to go with two pseudocubic unit cells along each in-plane direction x_2, x_3 to accommodate the local nonzero alternating rotation angles $\phi_i(x_1)$. In contrast, not to put any bias on the width of the resulting DW profile, the x_1 dimension of an appropriate supercell should be extremely elongated. Taking into account that in the chosen geometry the OP component $\phi_3(x_1)$ changes its sign when passing through the center of an APB at $x_1 = 0$, which corresponds to a phase shift of $\pm\pi$, we must choose an odd total number of pseudocubic unit cell parameters a_0 in the $\pm x_1$ direction. Potentially, this setup may conflict with the alternating periodicity of the OP components $\phi_1(x_1)$, $\phi_2(x_1)$, unless these components

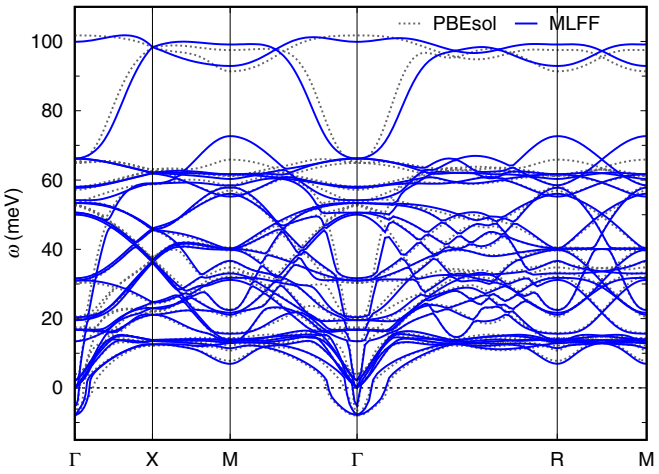

FIG. 1. Comparison of calculated phonon dispersions in the tetragonal $I4/mcm$ structure as determined directly from the PBEsol exchange-correlation functional (dotted lines) and using the MLFF (full lines).

vanish identically, which, however, is exactly required inside the bulk tetragonal domains separated asymptotically by the DW.

The structural relaxations of the DWs are performed using supercells with periodic boundary conditions containing an initial structural guess for a single APB at its center that is subsequently relaxed to the equilibrium structure. As explained above, this requires an odd number of pseudocubic unit cells in the x_1 direction. Following numerous careful tests, we adopt supercells of dimensions $59 \times 2 \times 2$, such that each supercell contains 1180 atoms. Guided by the results of Ref.

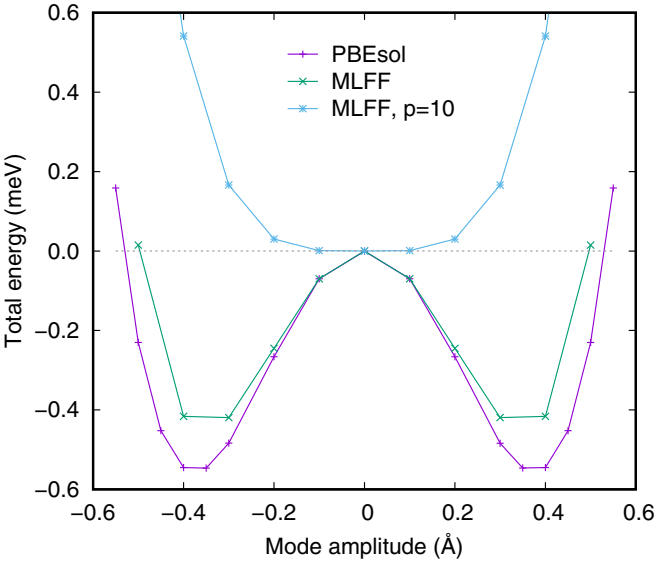

FIG. 2. Energy double well for the mode amplitude Γ_3 at $p = 0$ along the displacement pattern $\boldsymbol{E}_3$ in the bulk $I4/mcm$ phase calculated directly from DFT using the PBEsol exchange-correlation functional and from the MLFF. We find that using our MLFF, the FE instability disappears at $p^{(\mathrm{MLFF})} = 10$ kbar (blue line in the plot), while in DFT stabilization sets in at $p^{(\mathrm{DFT})} = 13$ kbar.

[28], we displace some of the atoms from their ideal cubic perovskite positions by performing alternating displacements of the transverse O_x and O_y oxygens along the x_2 and $-x_1$ directions, respectively, with an amplitude $\sim\bar{\phi}\tanh(x_1/\xi)$ resembling the octahedra rotations described by the OP ϕ_3. In addition, a Gaussian-shaped positive or negative hump around the DW with a somewhat smaller amplitude ϕ_1 is superimposed. Subject to hydrostatic pressures $p =$ 0, 10, 20, 40, 60, 80, 100, and 120 kbar, these initial candidate structures are relaxed while constraining the atoms in the boundary layers $x_1 = \pm 29\, a_0(p)$ to remain in their ideal bulk positions until forces on each atom have dropped below 0.001 eV/Å. To exclude the possibility of artifacts due to an insufficient size of the supercell, the resulting relaxed structures were also compared to those produced by completely unconstrained relaxations, with no significant differences found.

Taking the relaxed set of atomic positions as a deformation of the ideal cubic structure, we compute the resulting set of (mass-weighted) atomic displacement vectors [40] at each supercell lattice site $\boldsymbol{x}$ and locally project them onto normalized phonon polarization vectors of the ideal cubic reference structure. In this way we can extract the local amplitudes $\phi_i(\boldsymbol{x})$, $i =$ 1, 2, 3 corresponding to the cubic AFD soft mode. Since we assume the DW to be flat, we average these profiles over the (x_2x_3) cross sections of our supercells to obtain x_1-dependent profiles $\phi_i(x_1) = \frac{1}{4}\sum_{x_2,x_3}\phi(x_1, x_2, x_3)$. The OP component $\phi_2(x_1)$, which is zero in the initialized structures described above, is observed to remain zero during the subsequent relaxations and will be ignored in what follows. In a similar way, we determine the local amplitudes $\Gamma_i(x_1)$, $i = 1, 2, 3$ of the lowest tetragonal FE soft mode and the local electric polarization components $P_i(x_1) = (e/\Omega_0)\sum_{\kappa\in\Omega_0}\sum_j Z^*_{\kappa,ij}u_{\kappa j}(x_1)$, where Z^*_κ are the Born effective charge tensors for atom κ and $u_{\kappa j}(x_1)$ denotes the cross section-averaged displacement of this atom in the Cartesian direction with respect to the tetragonal bulk reference structure. Technical details of how these procedures are implemented are provided in the Supplemental Material (SM) [41].

IV. ANALYSIS OF STRUCTURAL OP AND POLARIZATION AMPLITUDES

We begin by focusing on the local OP component ϕ_3. Its local profiles resemble tanh-like kinks passing through zero at the center of the supercells and are well fitted by functions $\bar{\phi}\tanh[(x_1/\xi)\exp(ax_1^2 + bx_1^4 + \dots)]$. The resulting widths $\delta(p) \equiv 2\xi(p)$, shown in Fig. 3(a), start out at approx. $15\, a_0(p = 0)$ at ambient pressures but are observed to narrow under increasing external pressure to about $5\, a_0(p)$ at $p = 120$ kbar.

In Ref. [20], the Euler-Lagrange equations of LGD for a hard wall were formulated at zero pressure $p = 0$ and studied with analytical approximations. To compare the results of our atomistic simulations to the predictions of LGD theory quantitatively, we instead solve these equations numerically but without any approximations, which yields a corresponding DW width of $\delta \approx 21\, a_0(0)$. Even if one takes into account that pressure scales derived from different exchange-correlation functionals may not be directly comparable in a one-to-one manner, this is certainly in much better agreement with the

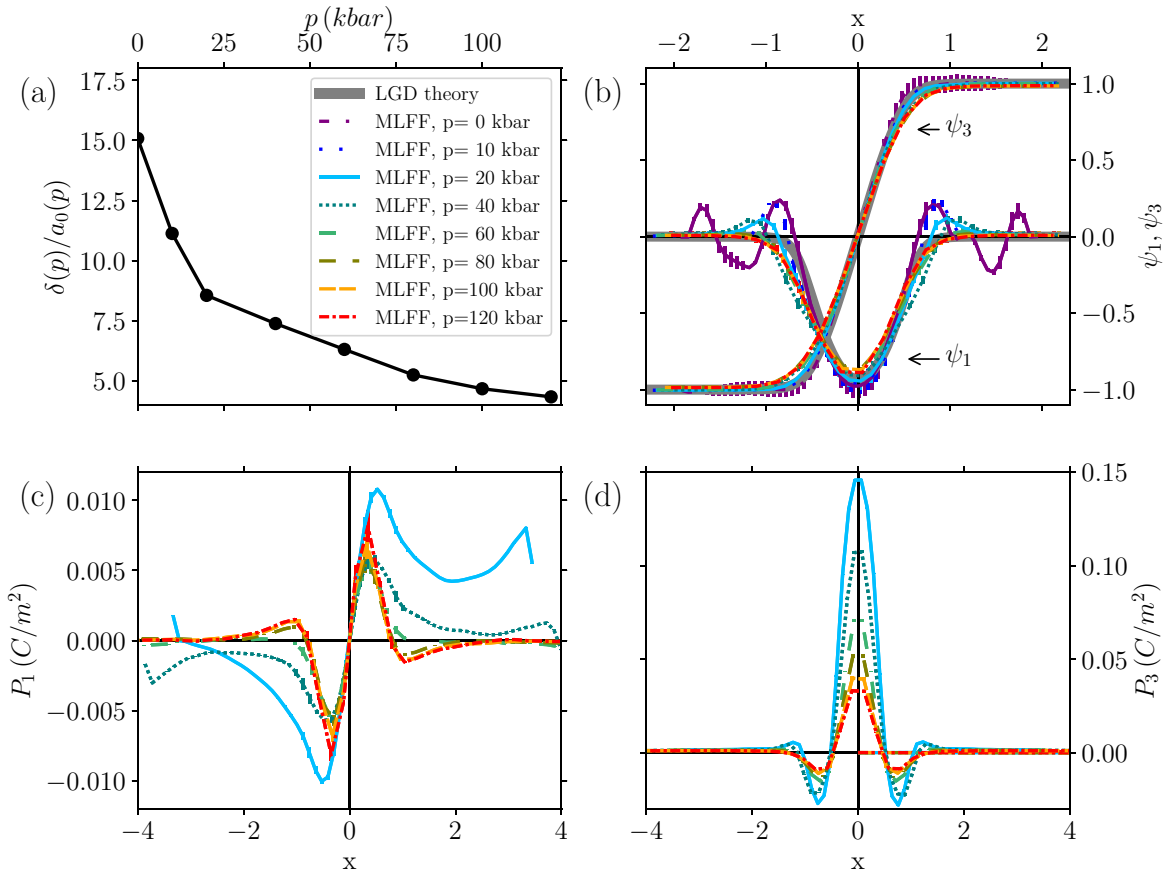

FIG. 3. (a) Pressure dependence of the DW width $\delta(p)$ measured in units of the pseudocubic lattice constant $a_0(p)$. (b) Comparison of rescaled OP profiles $\psi_1(x)$ and $\psi_3(x)$ as obtained from our MLFF simulations at pressures $p = 0, 10, 20, 40, 60, 80, 100$, and 120 kbar (colored) and numerical solutions of LGD theory (gray). As explained in the text, distances x_1 are measured in units of the DW width $\delta(p)$, i.e., $x_1 \equiv x \cdot \delta(p)$, and OP components ϕ_i are normalized with respect to the bulk OP modulus $\bar{\phi}(p)$, i.e., $\psi_i(x) = \phi_i(x\delta(p))/\bar{\phi}(p)$. (c), (d) Polarization profiles $P_1(x)$ and $P_3(x)$, respectively, for pressures $p = 20, 40, 60, 80, 100$, and 120 kbar. Polarization profiles for unstable configurations at $p = 0$ kbar and $p = 10$ kbar were found to be completely out of scale and were thus deliberately omitted from the plot.

low-pressure values obtained from our MLFF simulations [Fig. 3(a)] than a value $\delta(0) \approx 5.8\, a_0(0)$ resulting from a fit of the data shown in Fig. 3 of Ref. [28].

For the following discussion, it will be convenient to parametrize distances $x \equiv x_1/\delta(p)$ in units of the corresponding DW widths δ and to normalize all OP profiles $\psi_i(x) \equiv \phi_i(x\delta)/\bar{\phi}$ with respect to the corresponding bulk OP modulus value $\bar{\phi}$. Remarkably, as demonstrated in Fig. 3(b), for all pressures $p \geqslant 10$ kbar the rescaled profiles $\psi_1(x)$ and $\psi_3(x)$ obtained from MLFF simulations nicely collapse onto the two equally rescaled numerical solutions $\psi_1(x)$, $\psi_3(x)$ obtained from LGD theory using the parametrization of Ref. [20], respectively. In particular, in perfect accordance with the prediction of LGD theory, the amplitudes $\phi_1(x = 0)$ at the DW center calculated with MLFFs reach about 93% of the bulk value $\bar{\phi}$, which, however, completely disagrees with the much smaller amplitude observed in Ref. [28]. At variance with results for higher pressure, however, Fig. 3(b) reveals that for low pressures the OP profiles of the component $\phi_1(x_1)$ appear to deviate from those of ideal localized humps confined to the region inside the DW. Instead, pronounced oscillations, which are strongest for $p = 0$, are also observed throughout the hypothetical bulk regions, signaling an instability of the tetragonal bulk phase. To some extent, this behavior is to be expected [42]. Within the Born-Oppenheimer approximation, the tetragonal phase presents a FE instability, which is indicated by the presence of imaginary phonon modes at the Γ point (cf. Fig. 1).

Hence, performing a structural relaxation with a sufficiently small force relaxation threshold, one is bound to detect and follow these unstable directions, thereby disrupting the $I4/mcm$ bulk domains in favor of energetically lower lying states. It is, however, well-known (cf., e.g., Refs. [24,43]) that in the cubic phase there is a competition between R_{25} and the lowest Γ_{15} modes so under increasing pressure the former softens while the latter hardens. Already at an external hydrostatic pressure of $p = 10$ kbar the above mentioned double well turns into a stable, albeit shallow potential, and the local OP profile $\phi_1(x_1)$ becomes much more confined to the vicinity of the DW (cf. Fig. 2).

Around the distances $x_1 = \pm\delta(p)$ from the DW center, however, residual traces of these anomalies are found to survive in $\phi_1(x_1)$ even for pressures up to about 40 kbar in Fig. 3(b). These side wiggles still hint at a residual activation of the unstable Γ_{15} modes due to coupling with the local anisotropic strain accompanying the onsets of the DW. Of

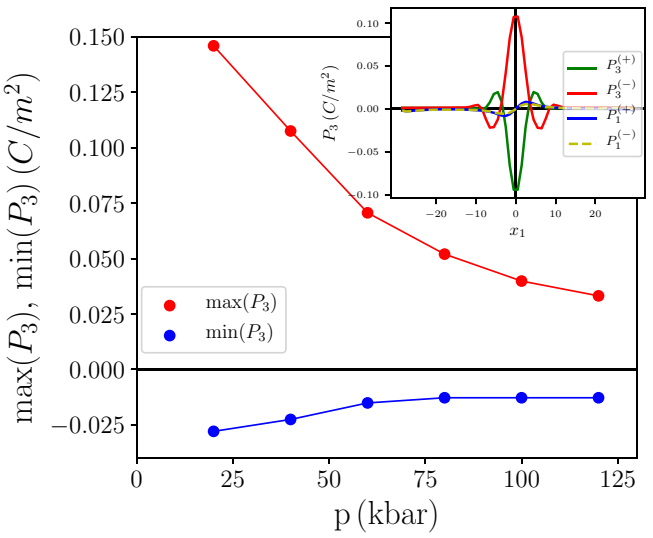

FIG. 4. Pressure evolution of the extrema of the polarization profile $P_3(x)$. Inset: Polarization profiles $P_1(x_1)$ and $P_3(x_1)$ for $\phi_1(x)\phi_3'(x) < 0$ (label +) and $\phi_1(x)\phi_3'(x) > 0$ (label –) at pressure $p = 40$ kbar.

course, the observed stabilization of the tetragonal bulk phase of STO with increasing pressure can also be monitored directly in terms of the profiles $\Gamma(x_1)$ of the unstable Γ_{15}-mode amplitudes (see the SM [41]).

Turning to the components of the local electric polarization vector $P_i(x_1)$, inside the DWs nonzero symmetric polarizations $P_3(x_1) = P_3(-x_1)$ and asymmetric components $P_1(x_1) = -P_1(-x_1)$ are seen to emerge [Figs. 3(c) and 3(d)], while $P_2(x_1)$ vanishes identically (not shown). All these findings are in perfect agreement with layer group symmetry analysis [44]. The observed overall sign of the polarization is, however, found to be fully determined by the particular OP profiles realized, an observation that has profound consequences for LGD theory. To appreciate this, recall that due to the alternating nature of the R_{25} phonon displacement patterns, the overall signs of the individual amplitudes $\phi_i(x_1)$ resulting from our analysis of supercell data are not well defined, but that of the product $\phi_1(x_1)\phi_3'(x_1)$ is. Indeed, when performing MLFF relaxations with a flipped sign of the initial profile guess $\phi_1^{(\mathrm{init})}(x_1)$, the relaxation always yielded a final configuration in which both the symmetric profiles $\phi_1(x_1)$ and $P_3(x_1)$ were exactly reversed, while the asymmetric profile $P_1(x_1)$ remained invariant (see inset of Fig. 4). Interestingly, while the symmetry $\{\pm\phi_1, \phi_3\}$ is in full accordance with the corresponding symmetry of the underlying LGD free energy G_ϕ (Eq. (1) of Ref. [20]), the terms listed in the polarization-dependent LGD free-energy contribution G_P as listed in Eqn. (43) of Ref. [20] do not allow us to decide whether a sign flip of $\phi_1(x_1)$ will be compensated by $\{P_1, P_3\} \to \{-P_1, P_3\}$ or by $\{P_1, P_3\} \to \{P_1, -P_3\}$. Since the strain tensor is invariant under a change of sign of ϕ_1, so-called flexoelectric terms [19] that couple polarization gradients to strain tensor components also fail to provide any criterion to decide this question. However, consider the so-called rotopolar coupling terms [44,45]

$$
\begin{aligned}
G_R = {} & W_1\left[P_1\left(\frac{\partial\phi_1}{\partial x_3}\phi_3 + \frac{\partial\phi_1}{\partial x_2}\phi_2\right) + P_2\left(\frac{\partial\phi_2}{\partial x_3}\phi_3 + \frac{\partial\phi_2}{\partial x_1}\phi_1\right) + P_3\left(\frac{\partial\phi_3}{\partial x_1}\phi_1 + \frac{\partial\phi_3}{\partial x_2}\phi_2\right)\right] \\
& + W_2\left[P_1\left(\frac{\partial\phi_2}{\partial x_2}\phi_1 + \frac{\partial\phi_3}{\partial x_3}\phi_1\right) + P_2\left(\frac{\partial\phi_1}{\partial x_1}\phi_2 + \frac{\partial\phi_3}{\partial x_3}\phi_2\right) + P_3\left(\frac{\partial\phi_1}{\partial x_1}\phi_3 + \frac{\partial\phi_2}{\partial x_2}\phi_3\right)\right] \\
& + W_3\left[P_1\left(\frac{\partial\phi_3}{\partial x_1}\phi_3 + \frac{\partial\phi_2}{\partial x_1}\phi_2\right) + P_2\left(\frac{\partial\phi_3}{\partial x_2}\phi_3 + \frac{\partial\phi_1}{\partial x_2}\phi_1\right) + P_3\left(\frac{\partial\phi_1}{\partial x_3}\phi_1 + \frac{\partial\phi_2}{\partial x_3}\phi_2\right)\right] \\
& + W_4\left[P_1\frac{\partial\phi_1}{\partial x_1}\phi_1 + P_2\frac{\partial\phi_2}{\partial x_2}\phi_2 + P_3\frac{\partial\phi_3}{\partial x_3}\phi_3\right],
\end{aligned}
\tag{1}
$$

which involve four independent coupling constants W_i, $i = 1, \ldots, 4$. For a purely $x_1 \equiv x$-dependent problem they reduce to

$$
\begin{aligned}
G_R = {} & W_1\left(P_2\frac{\partial\phi_2}{\partial x} + P_3\frac{\partial\phi_3}{\partial x}\right)\phi_1 + W_2(P_2\phi_2 + P_3\phi_3)\frac{\partial\phi_1}{\partial x} \\
& + \frac{P_1}{2}\left(W_3\frac{\partial(\phi_2^2 + \phi_3^2)}{\partial x} + W_4\frac{\partial(\phi_1^2)}{\partial x}\right).
\end{aligned}
\tag{2}
$$

Neglecting the OP component ϕ_2, this simplifies to

$$
\begin{aligned}
G_R = {} & \left(W_1\frac{\partial\phi_3}{\partial x}\phi_1 + W_2\frac{\partial\phi_1}{\partial x}\phi_3\right)P_3 \\
& + \frac{P_1}{2}\left(W_3\frac{\partial(\phi_3^2)}{\partial x} + W_4\frac{\partial(\phi_1^2)}{\partial x}\right)
\end{aligned}
\tag{3}
$$

The two contributions to this expression may be regarded as bilinear couplings of P_3 and P_1 to the respective components of some local effective electric field mediated by the OP. However, while the effective field component that couples to P_1 is obviously quadratic in the OP components ϕ_i, the component $W_1\frac{\partial\phi_3}{\partial x}\phi_1 + W_2\frac{\partial\phi_1}{\partial x}\phi_3$ that couples to P_3 changes its sign upon flipping the sign of either ϕ_1 or ϕ_3. This term is precisely the type of coupling that is capable of inducing the switching behavior observed in our simulations. Additional evidence for the presence of such rotopolar couplings may be found in Fig. 4, as both the central maximum as well as the side minima seen in the profiles $P_3(x_1)$ show no tendency to decay to zero, much like the magnetization in an Ising model never drops to zero in the presence of a small added magnetic field.

There is evidence that rotopolar couplings of the general type $W_1 \neq W_2$ are indeed present in STO. As previously asserted by Schiaffino and Stengel [46], they should also play an

important role in understanding the polarization in ferroelastic walls, where they are reminiscent of the mechanism underlying the emergence of spontaneous polarization in cycloidal magnetic systems. Indeed, general rotopolar couplings break the inversion symmetry of a periodic sequence of ferroelastic DWs (e.g., of the type $3_1 \rightarrow 1_1 \rightarrow 3_2$), leading to a macroscopic polarization of such an arrangement. In view of the OP value $(0.93\bar{\phi}, 0, 0)$ at its center, the Néel-type profile $3_1 \rightarrow (\phi_1(x), 0, \phi_3(x)) \rightarrow 3_2$ that we obtained resembles a structure extremely close to such a sequence of ferroelastic twins, indicating that rotopolar terms play a similar role also here. In passing, we note that our full set of rotopolar couplings (1) reduces to restricted set of invariants given in Eq. (2a) of Ref. [47] upon constraining $W_1 = W_2$.

V. PRELIMINARY RESULTS OF MD SIMULATIONS

In principle, the possibility to carry out MD simulations to incorporate finite temperature effects to check the thermal stability of our zero temperature results seems evident once a precise ML force field is available. Probably the most important open question concerns the investigation of the thermal stability of the Néel-type OR profiles and the accompanying polarization patterns. Below we discuss preliminary results obtained from MD simulations based on our MLFFA. However, a thorough investigation of this topic would certainly call for new, substantial efforts well beyond the scope of the present paper.

For the purpose of MD, the 2×2 supercell diameter that we had used for our $T = 0$ K is clearly insufficient. In a first attempt, we replaced it with a larger 4×4 one. To mimic the effects of quantum fluctuations, we introduced a barostat that imposes a 20 kbar background pressure. To this setup, we added a Nosé-Hoover thermostat to maintain the desired temperature. The supercells were initialized from the relaxed DW configuration obtained at zero temperature. To prevent artifacts stemming from the odd number of unit cells in the x direction, atoms were fixed at the left and right supercell boundaries. With this rather minimalistic setup, we ran MD at temperatures $T = 30$, 50, and 80 K. OP profiles and polarizations resulting from these MD trajectories were analyzed using the same methodology already discussed above and in the SM [41], time averages of the polarization profiles (centered around the fluctuating DW center) were taken over the whole available trajectory length, and we compiled movies of each run that are supplied in the SM [41]. Let us briefly discuss our preliminary results obtained in this way.

(1) At $T = 30$ K, we observe that the Néel type of OP profile we obtained at $T = 0$ persists over the whole trajectory length of 61 ps. The time-averaged centered polarization profiles display a structure that still remotely resembles the shape we found at $T = 0$, albeit at a somewhat reduced amplitude. In particular, even the asymmetric shape of $P_1(x)$ can still be observed remarkably well [cf. the movie `NpT_59x4x4_P20kbar_T30K.mp4` included in the SM and Fig. 5(a)].

(2) At $T = 50$ K, similar comments still apply, but at a much higher level of fluctuations. Averaging over configurations along an MD trajectory of length 124 ps, we observe a further reduction of polarization amplitudes [movie `NpT_59x4x4_P20kbar_T50K.mp4` included in the SM and Fig. 5(b)].

(3) Running MD at $T = 80$ K for 117 ps, one can still recognize a tendency toward preserving a Néel character of the OP profiles, but the polarization profile shows an increased tendency to disintegrate [movie `NpT_59x4x4_P20kbar_80TK.mp4` included in the SM and Fig. 5(c)].

(4) The observed reduction of the maximum of the amplitude of $P_3(x)$ with increasing temperature is shown in Fig. 5(d). Note the similarity of this behavior with respect to temperature to the pressure dependence of the maximum of $P_3(x)$ as observed in Fig. 4. We regard this as further evidence for the presence of the rotopolar couplings discussed above.

Despite all this encouraging evidence, at the present stage we must still regard the above observations as preliminary. To obtain conclusive results would certainly at least require several adjustments to the current setup which will increase the computational costs of such simulations drastically:

(1) The small 4×4 cross section effectively cuts off all but the largest wavelength fluctuation of capillary modes traveling parallel to the DW, probably at the expense of seriously underestimating thermal broadening of the DW. At the same time, for such a small supercell diameter the free energy barriers from a Néel profile to other metastable DW configurations (e.g., a Néel profile with reversed sign of ϕ_1 or a Bloch type profile) may easily be crossed, thus erroneously indicating instability at a given temperature and timescale.

(2) To get rid of the constraint of fixing atoms at the boundary, which is certainly not desirable in MD, the supercell must be replaced by one with an even number of unit cells in each direction, which is only possible if it hosts two opposite DWs instead of a single one, further increasing its size.

(3) On top of this, investigations at low temperatures in principle require inclusion of nuclear quantum fluctuations [48]. While we have mimicked these effects here by introducing a stabilizing background pressure, a more stringent approach would call for performing, e.g., a path integral MD simulation, in which machine-learned potentials are combined with established quantum MD simulation techniques [49], further increasing the costs of such simulations by one or two orders of magnitude.

Clearly, each of these steps must be planned and tested carefully and will require massive computational resources. Work in this direction is currently underway in our group.

VI. DISCUSSION AND CONCLUSIONS

In summary, our paper highlights the exceptional agreement and mutual fruitful exchange between traditional symmetry-based LGD approaches and atomistic simulations of DWs based on ML methods. Using MLFFs trained on accurate DFT calculations, we were able to perform truly realistic simulations of hard APBs hosted by STO supercells requiring sizes that were previously out of reach for standard *ab initio* approaches. Our results are in remarkable agreement with predictions of LGD theory on a qualitative and even quantitative level. In particular, for a DW geometry normal to the x_1 direction, we observe a DW of Néel type, whose

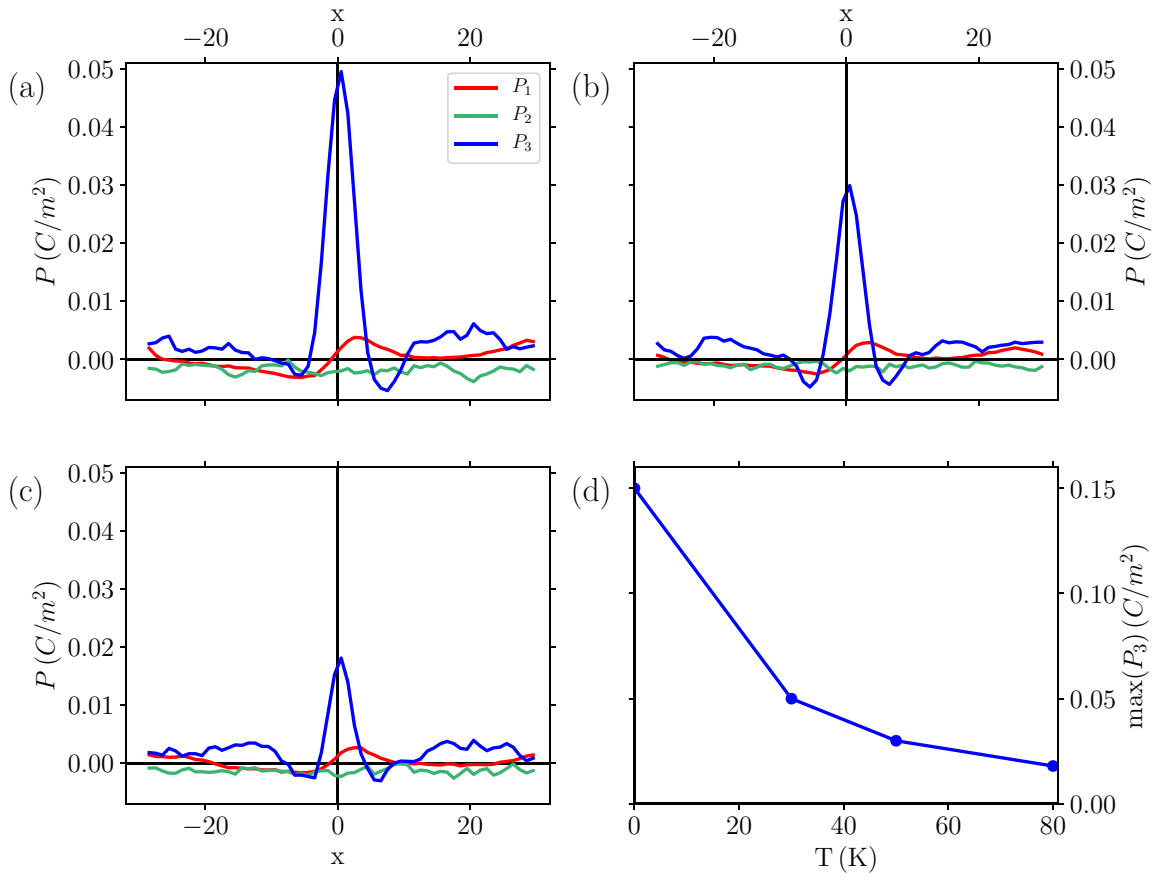

FIG. 5. Polarization profiles $P_1(x)$ (red), $P_2(x)$ (green), and $P_3(x)$ (blue) for (a) $T = 30$ K, (b) $T = 50$ K, and (c) $T = 80$ K; (d) temperature evolution of maxima of polarization component $P_3(x)$.

width δ and OP amplitude ϕ_1 are much larger than reported in Ref. [[28]] and are in excellent agreement with our numerical solutions of LGD theory. To the best of our knowledge, it is hard to find better examples of agreement of LGD and *ab initio* results anywhere in the DW literature. We also observe that the DW carries a dominant symmetric $P_3(x_1)$ in-plane polarization component and a smaller asymmetric normal component $P_1(x_1)$. The observed symmetry properties and pressure dependence of the OP and polarization profiles are compatible with the presence of rotopolar couplings. Both in terms of reachable system sizes and ease of including finite temperature effects by, e.g., MD or Monte Carlo while maintaining DFT-like accuracy, ML-based methods will lead to a huge step forward in the computational study of DWs in the near future.

ACKNOWLEDGMENTS

A.T. acknowledges support by the Austrian Science Fund (FWF) Project No. P27738-N28, and C.V., C.D., and G.K. by FWF Project No. F81-08 (SFB TACO).

[1] J. Valasek, Phys. Rev. **17**, 475 (1921).
[2] V. K. Wadhawan, *Introduction to Ferroic Materials* (Gordon and Breach, Amsterdam, 2000).
[3] L. C. A. K. Tagantsev and J. Fousek, *Domains in Ferroic Crystals and Thin Films* (Springer, New York, 2010).
[4] D. Meier and S. M. Selbach, Nature Reviews Materials **7**, 157 (2022).
[5] D. Meier, J. Seidel, M. Gregg, and R. Ramesh, *Domain Walls: From Fundamental Properties to Nanotechnology Concepts* (Oxford University Press, Oxford, UK, 2020).
[6] H. Béa and P. Paruch, Nat. Mater. **8**, 168 (2009).
[7] P. Sharma, P. Schoenherr, and J. Seidel, Materials **12**, 2927 (2019).
[8] G. Nataf and M. Guennou, J. Phys.: Condens. Matter **32**, 183001 (2020).
[9] T. Sluka, A. K. Tagantsev, P. Bednyakov, and N. Setter, Nat. Commun. **4**, 1808 (2013).
[10] Y. Kim, M. Alexe, and E. Salje, Appl. Phys. Lett. **96**, 032904 (2010).
[11] S. Van Aert, S. Turner, R. Delville, D. Schryvers, G. Van Tendeloo, and E. K. Salje, Adv. Mater. **24**, 523 (2012).
[12] H. Yokota, H. Usami, R. Haumont, P. Hicher, J. Kaneshiro, E. K. H. Salje, and Y. Uesu, Phys. Rev. B **89**, 144109 (2014).
[13] H. Yokota, S. Niki, R. Haumont, P. Hicher, and Y. Uesu, AIP Adv. **7**, 085315 (2017).
[14] E. K. H. Salje, O. Aktas, M. A. Carpenter, V. V. Laguta, and J. F. Scott, Phys. Rev. Lett. **111**, 247603 (2013).

[15] E. K. Salje, M. Alexe, S. Kustov, M. C. Weber, J. Schiemer, G. F. Nataf, and J. Kreisel, Sci. Rep. **6**, 27193 (2016).
[16] G. Nataf, M. Guennou, J. Gregg, D. Meier, J. Hlinka, E. Salje, and J. Kreisel, Nat. Rev. Phys. **2**, 634 (2020).
[17] G. Catalan, J. Seidel, R. Ramesh, and J. F. Scott, Rev. Mod. Phys. **84**, 119 (2012).
[18] P. Sharma, Q. Zhang, D. Sando, C. H. Lei, Y. Liu, J. Li, V. Nagarajan, and J. Seidel, Sci. Adv. **3**, e1700512 (2017).
[19] A. N. Morozovska, E. A. Eliseev, M. D. Glinchuk, L.-Q. Chen, and V. Gopalan, Phys. Rev. B **85**, 094107 (2012).
[20] A. K. Tagantsev, E. Courtens, and L. Arzel, Phys. Rev. B **64**, 224107 (2001).
[21] R. Cowley, Philos. Trans. R. Soc. London A **354**, 2799 (1996).
[22] *Physics of Ferroelectrics*, Topics in Applied Physics, Vol. 105, edited by K. Rabe, C. Ahn, and J.-M. Triscone (Springer, Berlin, 2007).
[23] K. A. Müller and H. Burkard, Phys. Rev. B **19**, 3593 (1979).
[24] R. Wahl, D. Vogtenhuber, and G. Kresse, Phys. Rev. B **78**, 104116 (2008).
[25] B. Houchmandzadeh, J. Lajzerowicz, and E. Salje, J. Phys.: Condens. Matter **3**, 5163 (1991).
[26] V. Janovec and V. V. Dvořák, Ferroelectrics **66**, 169 (1986).
[27] V. Janovec and J. Přívratská, in *International Tables for Crystallography*, edited by A. Authier (Kluwer Academic Publishers, Dordrecht/Boston/London, 2003), Vol. D, Chap. 3.4, pp. 449–505.
[28] A. Kvasov, A. K. Tagantsev, and N. Setter, Phys. Rev. B **94**, 054102 (2016).
[29] V. L. Deringer, A. P. Bartók, N. Bernstein, D. M. Wilkins, M. Ceriotti, and G. Csányi, Chem. Rev. **121**, 10073 (2021).
[30] P. Friederich, F. Häse, J. Proppe, and A. Aspuru-Guzik, Nat. Mater. **20**, 750 (2021).
[31] R. Jinnouchi, J. Lahnsteiner, F. Karsai, G. Kresse, and M. Bokdam, Phys. Rev. Lett. **122**, 225701 (2019).
[32] R. Jinnouchi, F. Karsai, and G. Kresse, Phys. Rev. B **100**, 014105 (2019).
[33] R. Jinnouchi, F. Karsai, C. Verdi, R. Asahi, and G. Kresse, J. Chem. Phys. **152**, 234102 (2020).
[34] A. P. Bartók, M. C. Payne, R. Kondor, and G. Csányi, Phys. Rev. Lett. **104**, 136403 (2010).
[35] R. Jinnouchi, K. Miwa, F. Karsai, G. Kresse, and R. Asahi, J. Phys. Chem. Lett. **11**, 6946 (2020).
[36] G. Kresse and J. Hafner, Phys. Rev. B **47**, 558 (1993).
[37] G. Kresse and J. Furthmüller, Phys. Rev. B **54**, 11169 (1996).
[38] A. Togo and I. Tanaka, Scr. Mater. **108**, 1 (2015).
[39] A. P. Bartók, R. Kondor, and G. Csányi, Phys. Rev. B **87**, 184115 (2013).
[40] G. Eckold, in *International Tables for Crystallography*, edited by A. Authier (Kluwer Academic Publisher, Dordrecht/Boston/London, 2003), Vol. D, Chap. 2.1, pp. 286–313.
[41] See Supplemental Material at http://link.aps.org/supplemental/10.1103/PhysRevMaterials.6.094408 for Sec. S1, "Details of our analysis of DW profiles," as well as three movies compiled from our MD simulations. The Supplemental Material also contains Refs. [50,51].
[42] N. Sai and D. Vanderbilt, Phys. Rev. B **62**, 13942 (2000).
[43] U. Aschauer and N. A. Spaldin, J. Phys.: Condens. Matter **26**, 122203 (2014).
[44] W. Schranz, C. Schuster, A. Tröster, and I. Rychetsky, Phys. Rev. B **102**, 184101 (2020).
[45] W. Schranz, A. Tröster, and I. Rychetsky, J. Appl. Phys. **128**, 194101 (2020).
[46] A. Schiaffino and M. Stengel, Phys. Rev. Lett. **119**, 137601 (2017).
[47] E. A. Eliseev, S. V. Kalinin, Y. Gu, M. D. Glinchuk, V. Khist, A. Borisevich, V. Gopalan, L.-Q. Chen, and A. N. Morozovska, Phys. Rev. B **88**, 224105 (2013).
[48] W. Zhong and D. Vanderbilt, Phys. Rev. Lett. **74**, 2587 (1995).
[49] T. E. Markland and M. Ceriotti, Nat. Rev. Chem. **2**, 0109 (2018).
[50] P. Ghosez, J.-P. Michenaud, and X. Gonze, Phys. Rev. B **58**, 6224 (1998).
[51] W. Zhong, R. D. King-Smith, and D. Vanderbilt, Phys. Rev. Lett. **72**, 3618 (1994).